actuators

MDPI

Article

Wound-Rotor Synchronous Motor with Toroidal Windings for UAV Propulsion Systems

Se-Eun Kim and Yong-Min You *

Department of Future Mobility Convergence, Chonnam National University, Gwangju 61186, Republic of Korea; kse23@jnu.ac.kr

* Correspondence: ym.you@jnu.ac.kr; Tel.: +82-62-530-4229

Abstract

Recently, unmanned aerial vehicles (UAVs) based on electric propulsion systems are being increasingly adopted in various fields, including industrial and military applications. Outer-rotor surface-mounted permanent magnet synchronous motors (SPMSMs) are predominantly applied in UAV propulsion systems. However, these motors are vulnerable to the price fluctuations of rare-earth materials and supply chain instability. In addition, the magnets in these motors are prone to detachment at high rotational speeds, and demagnetization under high-temperature conditions may reduce output performance. To address these limitations, research is being actively conducted on non-permanent magnet motors, among which, wound-rotor synchronous motors (WRSMs) offer the advantage of controllable field excitation at high speeds. Furthermore, WRSMs can use both magnetic and reluctance torques, thereby increasing power density relative to other non-permanent magnet motors. However, the adoption of an additional field winding increases copper loss, thus reducing motor efficiency. This study investigates the application of the toroidal winding structure, which is already widely applied in permanent magnet and brushless direct current machines, to WRSMs. The performance of these motors is compared with that of motors using conventional tooth-coil windings. The toroidal windings are circumferentially distributed along both the inner and outer stator yoke paths, effectively reducing the end-turn length relative to that of conventional tooth-coil windings. Two WRSMs, one with tooth-coil and another with toroidal windings, are designed using identical specifications to compare performances via finite element analysis. The armature copper loss in the proposed model decreased by approximately 28% because the toroidal winding structure reduced the end-turn length. As a result, the efficiency increased by about 1.9% due to the reductions in copper, core, and eddy current losses.

Keywords: unmanned aerial vehicles; wound-rotor synchronous motors; tooth-coil winding; toroidal winding; finite element analysis; motor efficiency

Check for updates

Academic Editors: Paolo Mercorelli, Lihui Wang, Bailing Tian and Hongyang Bai

Received: 14 November 2025
Revised: 29 December 2025
Accepted: 15 January 2026
Published: 1 February 2026

Copyright: © 2026 by the authors. Licensee MDPI, Basel, Switzerland. This article is an open access article distributed under the terms and conditions of the Creative Commons Attribution (CC BY) license.

1. Introduction

Unmanned aerial vehicles (UAVs), owing to their benefits such as low operating costs and minimized human risk, have been widely used in various fields, including industrial and military applications [1,2]. In particular, UAVs based on electric propulsion systems have recently attracted considerable attention, as these UAVs exhibit environmentally friendly and quiet characteristics [3]. Propulsion motors for UAVs must maintain stable performance across a wide range of operating conditions and ensure sufficient mechanical robustness, particularly during high-speed rotation. Furthermore, given the limited battery

capacity of electric propulsion UAVs and the increasing emphasis on environmentally friendly operation, the development of high-efficiency propulsion motors that minimize energy consumption and environmental impact is essential.

Permanent magnet synchronous motors (PMSMs), especially outer-rotor surface-mounted PMSMs (SPMSMs), are widely used in UAV propulsion systems to meet these requirements because of their high torque density and efficiency. However, SPMSMs have several limitations for long-term application due to various disadvantages. The cost and supply chain stability of SPMSMs are strongly affected by price fluctuations and geopolitical risks associated with rare-earth materials, and the extraction and processing of these materials impose considerable environmental burdens [4]. Furthermore, surface-mounted magnets are susceptible to magnet scattering at high rotational speeds if the rotor assembly lacks the mechanical robustness to withstand the centrifugal forces [5]. Moreover, the demagnetization of permanent magnets owing to temperature increases and an inverse magnetic field deteriorates motor performance, which directly influences flight safety [6]. These issues motivate the exploration of alternative motor technologies that can reduce rare-earth materials dependence while maintaining high efficiency and reliability.

Among non-permanent-magnet motors, switched reluctance motors (SRMs) are being proposed as propulsion motors for UAVs due to their structural simplicity, robustness, and excellent fault tolerance. The SRM was applied as the propulsion motor for a hybrid UAV [7]. The characteristic analysis conducted across various flight altitudes confirmed that the SRM satisfied the performance requirements under high speeds. However, the phase current was applied in a pulsed form, which can degrade system performance. In the study reported in [8], the characteristics of PMSMs and SRMs for drone propulsion motors were compared. Although both PMSMs and SRMs satisfied the same rated output, PMSMs demonstrated superior performance in terms of efficiency and torque ripple. A 4-phase SRM was proposed in [9] to enhance fault tolerance, and this SRM was confirmed to significantly improve fault-tolerant capability. Multi-phase SRM topologies have been proposed to enhance fault tolerance, but their relatively high torque ripple and lower efficiency remain significant drawbacks. Consequently, SRMs have limitations in their application as propulsion motors for UAVs, which demand stability and high efficiency.

Meanwhile, wound-rotor synchronous motors (WRSMs) are considered non-permanent magnet type motors that provide controllable field excitation. The WRSMs use the reluctance torque generated owing to the inductance difference and the magnetic torque generated owing to the mutual flux interaction of the field and armature current [10]. Consequently, WRSMs have the advantage of exhibiting a higher torque density than SRMs. Moreover, WRSMs can adjust the field flux based on the load and speed requirements [11]. This field controllability enables stable output characteristics over a wide operating range and offers flexibility for field-weakening and fault-handling strategies. However, a key drawback of WRSMs is their high copper loss owing to the use of field windings instead of permanent magnets, in the rotor. This loss not only reduces overall drive efficiency but also increases motor heating, which is particularly detrimental for systems requiring extended operation. To address this issue, previous studies have proposed various approaches such as optimal current control strategies to minimize copper loss in the field-weakening region, the application of grain-oriented electrical steel to enhance cross-magnetization utilization, and the adoption of hairpin-type rectangular conductors to improve slot fill factor and torque density [12–14]. Although these methods contribute to reducing copper loss, they do not fundamentally address the increased winding resistance resulting from long end-turns. As a result, the copper loss associated with the coil end-turn region remains a concern. Consequently, a winding method that structurally minimizes end-turn length is required to reduce copper loss and enhance the efficiency of WRSMs.

Toroidal winding represents one such method capable of structurally minimizing the end-turn length. In this configuration, the coil is wound uniformly in the circumferential direction around the inner and outer stator core yokes. Consequently, the end-turn length of the coil can be considerably shorter than that of the conventional tooth-coil winding, which reduces copper loss and enhances motor efficiency [15]. Toroidal windings have already been applied in several machine topologies to realize this end-turn reduction and the associated copper-loss improvement. In synchronous reluctance machine, permanent magnet machine and induction machine, toroidal stator windings have been reported to shorten the total winding length, which leads to lower armature copper loss, improved efficiency, and more compact designs [16–18]. However, despite these benefits, the application of toroidal winding has been largely restricted to the aforementioned machines.

In this study, copper loss that causes excessive heating in UAV propulsion WRSMs is reduced by replacing the conventional tooth-coil armature winding with a toroidal winding. To enable an objective comparison under identical design conditions, two WRSMs for UAV propulsion are designed, a conventional model with a tooth-coil winding and a proposed model with a toroidal winding. Section 2 outlines the WRSM design procedure based on torque per rotor volume, magnetic and electric loadings, and then defines identical motor specifications for the conventional and proposed models. It also details the geometric derivation of the stator core of the proposed model, demonstrating how the inner and outer slot areas are equalized by adjusting the back yoke position. Furthermore, this section compares the theoretical phase resistance of the two winding configurations. Section 3 analyzes the electromagnetic characteristics under no-load and load conditions through Finite Element Analysis (FEA) and validates the mechanical robustness of the rotor structure. Section 4 discusses the main differences between the two winding topologies and their impact on UAV propulsion performance. It details how the structural advantages of toroidal winding contribute to reduced copper loss and improved efficiency, while analyzing the trade-offs regarding electromagnetic behaviors. Finally, this study concludes in Section 5 with a summary of the findings.

2. Wound-Rotor Synchronous Motor Topology

2.1. Design Procedure

The motor size is calculated using the torque per unit rotor volume (TRV), which expresses the product of the magnetic and electric loadings [19], the primary parameters that determine the motor output. Magnetic and electric loadings refer to the average magnetic flux density generated in the air gap, and the linear current density along the air-gap circumference, respectively [20]. Although the increase in magnetic loading increases the magnetic flux density, the iron core becomes saturated. An increase in electric loading increases the torque; however, copper losses and temperature also increase. Therefore, the selection of the two loading values is crucial to designing a motor that maximizes torque and efficiency while minimizing loss and temperature increase within a limited volume [21]. Similarly to other AC machines, it is important to determine the major dimensions of the motor by considering both the electric and magnetic loadings, and the formulas used to calculate these loadings are expressed in Equations (1) and (2) [22,23]. In addition, the expression related to the total ampere-turns and the field current, which defines the magnetizing requirement of the machine, is formulated in Equations (6) and (7) [24].

$$\phi = B \times \frac{\pi D_a L}{2p}, \tag{1}$$

where ϕ is the magnetic flux per pole, B is the magnetic loading, D_a is the air-gap diameter, L is the axial stack length, and p is the number of pole pairs.

$$A = \frac{2mN_{ph}I}{\pi D_a}, \tag{2}$$

where A is the electric loading, m is the number of phases, N_{ph} is the number of armature series turns per phase, and I is the phase current.

The phase back EMF and torque are expressed in Equations (3) and (4), respectively. TRV is defined as the torque calculated using Equation (4), divided by the rotor volume, as per Equation (5).

$$E = \frac{\pi^2 k_w N_{ph} f D_a B L}{\sqrt{2}p}, \tag{3}$$

where E is the phase back EMF, k_w is the winding factor, and f is the electric frequency.

$$T = \frac{\pi^2 k_w A B {D_a}^2 L}{4\sqrt{2}}, \tag{4}$$

$$TRV = \frac{T}{V_r} = \frac{\pi k_w A B}{\sqrt{2}}, \tag{5}$$

where T is the torque and V_r is the rotor volume.

$$A_{tot} = A_p + A_g + A_t + 0.5 \cdot \left(A_{ry} + A_{sy}\right), \tag{6}$$

$$I_f = \frac{A_{tot}}{N_f}, \tag{7}$$

where A_{tot} is the total ampere turns, A_p, A_g, A_t, A_{ry}, and A_{sy} are the ampere turns required to magnetize the pole core, air-gap, stator teeth, rotor yoke, and stator yoke, respectively. I_f is the field current, N_f is the number of field winding turns.

2.2. Specifications of the Motor

In this study, a conventional model with tooth-coil winding and the proposed model with toroidal winding are designed as propulsion motors applicable to UAVs. The two motors have a 10-pole and 12-slot structure. When current is supplied to the field winding around the rotor teeth, a field flux is generated. The configurations of the two models are displayed in Figure 1, revealing that both models contain a rotor core, a stator core, and windings.

To conduct an objective comparative analysis, both models are designed based on identical design specifications. Moreover, the rotor structure and field winding specifications are identically designed for both models. The outer diameter, tooth width, and back yoke height of the stator core are identically designed for the armature. In addition, the winding specifications, such as an equal number of series turns per phase and the applied current, pertain to both models. The winding method used for both models is concentrated winding, and the winding current density is 10 A/mm^2, considering the forced air-cooling condition imposed by the propeller used during UAV operation. The target motor specifications to ensure propulsion performance are an average torque of 2.3 N·m at a rated speed of 3000 rpm. The maximum speed and battery voltage are 6000 rpm and 48 V, respectively, and these target specifications are listed in Table 1.

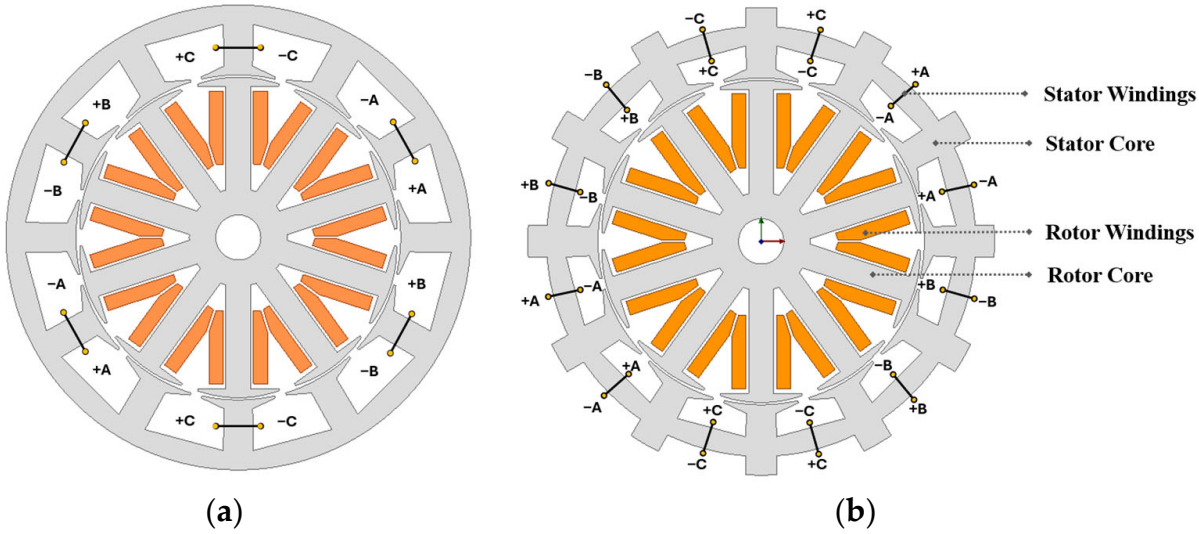

Figure 1. Structures of the WRSMs: (**a**) conventional and (**b**) proposed toroidal models.

Table 1. Design specifications of the conventional and proposed models.

Parameter		Unit	Value
Target specifications	DC voltage	V_{DC}	48
	Continuous power	W	720
	Continuous torque	N·m	2.3
	Rated speed	rpm	3000
	Maximum speed	rpm	6000
Material	Stator and rotor cores	-	35PN440
Mechanical	No. of poles and slots	ea	10/12
	Outer diameters of the stator and rotor	mm	103/55
	Outer diameter of the shaft	mm	10
	Air-gap	mm	0.5
	Lamination	mm	40
Electrical	Field current	A	10
	Armature current	A	26.5
	No. of turns per pole	Turns	45
	No. of series turns per phase	Turns	28

2.3. Calculation of the Stator Core Parameters of the Proposed Model

As mentioned in Section 2.2, the teeth width and back yoke height of the stator core are designed identically to objectively compare the conventional and proposed models. The slot area of the conventional model is given by Equation (8), and the stator of the proposed model is designed to equalize the inner and outer slot areas using Equations (9) and (10). In this design, the slot area of the conventional model is set to 150 mm^2, and the inner and outer slot areas of the proposed model are each configured as half of this value. The corresponding variables are presented in Figure 2 [25]. Owing to the design, the stator core volume of the proposed model is reduced by approximately 4.73% relative to that of the conventional model due to the adjustment of the back yoke position.

$$A_{c_in} = \pi\left[\left(\frac{D_o}{2} - h_y\right)^2 - \left(\frac{D_i}{2} + h_t\right)^2\right] - N_{slot} w_t \left(\frac{D_o}{2} - h_y - \frac{D_i}{2} - h_t\right), \quad (8)$$

$$A_{p_in} = \pi\left[\left(\frac{D_o}{2} - h_o - h_y\right)^2 - \left(\frac{D_i}{2} + h_t\right)^2\right] - N_{slot} w_t \left(\frac{D_o}{2} - h_o - h_y - \frac{D_i}{2} - h_t\right), \quad (9)$$

$$A_{p_out} = \pi\left[\left(\frac{D_o}{2}\right)^2 - \left(\frac{D_o}{2} - h_o\right)^2\right] - N_{slot} w_t h_o, \tag{10}$$

where A_{c_in} is the slot area of the conventional model, A_{p_in} and A_{p_out} are the inner and outer slot areas of the proposed model, respectively. Moreover, D_i and D_o are the inner and outer diameters of the stator, respectively, h_o is the outer tooth height, h_y is the height of the stator back yoke, h_t is the stator shoe height, N_{slot} is the number of slots, and w_t is the stator tooth width.

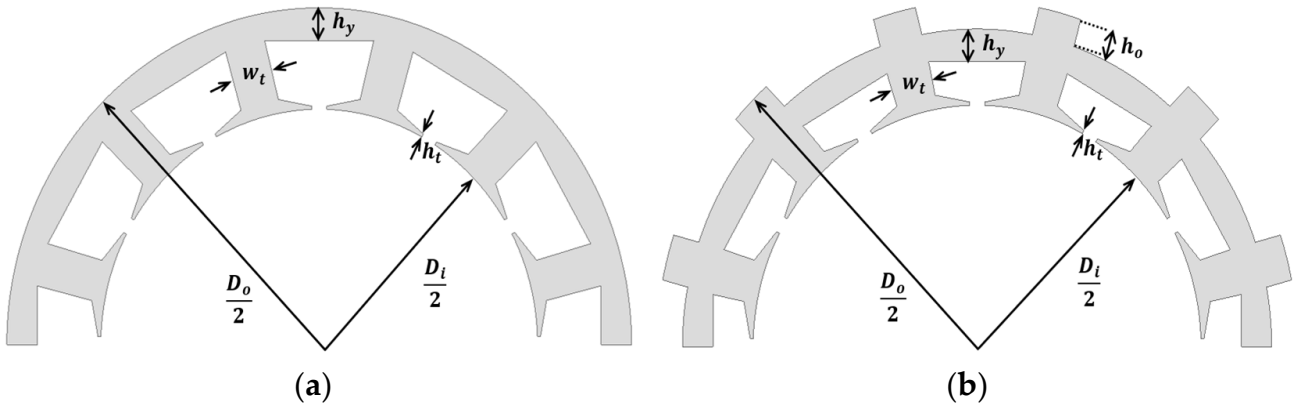

Figure 2. Stator core geometry and variables used for the (**a**) conventional model and (**b**) proposed model.

2.4. Phase Resistance of the Proposed Model

The concentrated winding method is applied to both the conventional and proposed models. As shown in Figure 3a,b, the winding configurations of the conventional and proposed models can be identified. The toroidal winding is arranged circumferentially around both the inner and outer sections of the stator core of the proposed model, as shown in Figure 3b. The half-turn length of both winding schemes depends on the geometric parameters of the motor. In the case of tooth-coil winding, the end-turn length significantly increases as the stator outer diameter increases or in motors with a small number of poles. In contrast, since the toroidal winding is arranged along the inner and outer yokes of the stator, it is advantageous when the stator yoke thickness is small relative to the pole pitch, or when reducing end-turn resistance is critical due to a short stack length. Figure 3c displays the cross-sectional view of one turn of the coil in the proposed model. The length of one coil turn is calculated using Equation (11), which is subsequently multiplied by the series turns per phase. Based on this, the total coil length per phase is calculated to be 3.35 m for the conventional model and 2.75 m for the proposed model. Next, the phase resistance of the armature winding is calculated using Equation (12) [26]. The calculation results revealed that the phase resistance of the proposed model was approximately 18% lower than that of the conventional model.

$$L_{total} = N_{ph}(4A + 2B + 2L), \tag{11}$$

$$R = \frac{L_{total}}{\sigma A_c}, \tag{12}$$

where L_{total} is the total coil length per phase, A and B are the height and width of the end-turn coil, respectively, R is the phase resistance of the coil, and σ and A_c is the electric conductivity and the cross-sectional area of the coil, respectively.

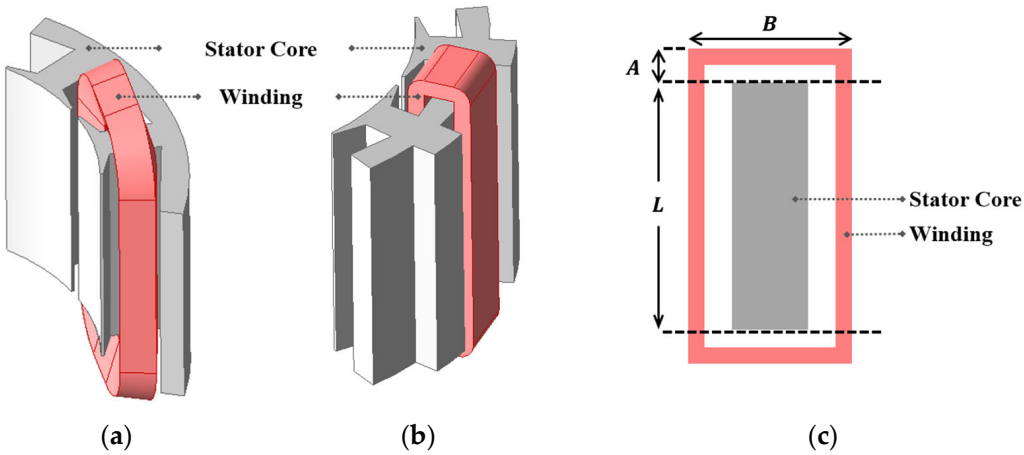

Figure 3. Winding configurations and cross-sections views: winding configurations of the (**a**) conventional model and (**b**) proposed model, and (**c**) cross-section corresponding to both windings.

3. FEA Results

3.1. No-Load Analysis Results

In this study, the electromagnetic characteristics of the two models were analyzed using the FEA software ANSYS Maxwell 2D, version 2024 R1. No-load analysis was conducted at the rated speed of 3000 rpm under field excitation conditions. Figure 4a,b display the phase back EMF waveforms obtained from the two models and the corresponding results of fast Fourier transform (FFT) analysis, respectively. The phase back EMF values of the conventional and proposed models were 10.2 V and 10.3 V, respectively, indicating comparable performance levels. FFT analysis provided fundamental and harmonic components, which were subsequently used to calculate the THD of the phase back EMF by applying Equation (13). The results revealed that the fundamental component of the proposed model was approximately 0.5% higher than that of the conventional model. However, the total magnitude of the harmonics, excluding the fundamental, was almost 50% higher than that of the conventional model. Consequently, the back EMF THD of the proposed model increased by 0.56% relative to that of the conventional model; however, the corresponding value was below 5%.

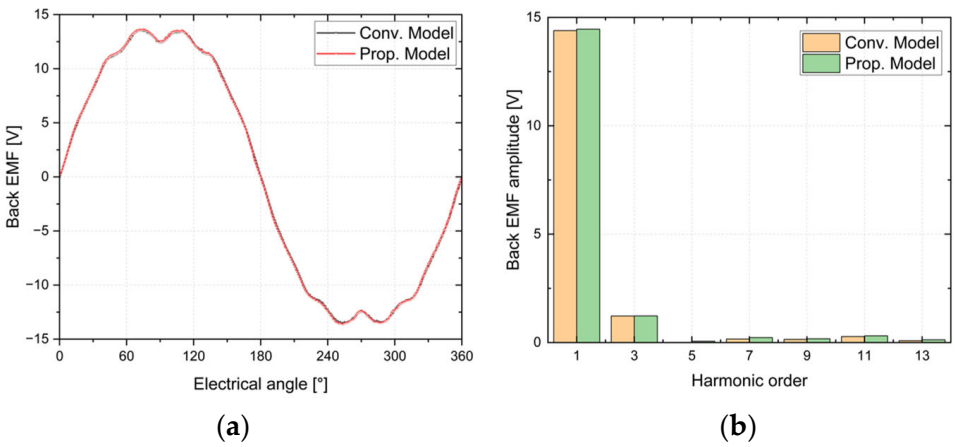

Figure 4. Comparison of the (**a**) phase back EMF waveforms and the (**b**) FFT results obtained from the two models.

Figure 5a presents the cogging torque waveforms of the two models. Cogging torque is generated by the variation in the air-gap magnetic reluctance as the rotor rotates. The periodicity of the cogging torque is inversely proportional to the least common multiple

(LCM) of the number of poles and slots. Equation (14) expresses the periodicity of the cogging torque. As both models have a 10-pole, 12-slot configuration, three cogging torque cycles occurred under 90° electrical rotation. The analysis results confirmed that the peak-to-peak values of the cogging torque obtained from the conventional and proposed models were 24.4 mN·m and 28.7 mN·m, respectively. This indicated that the value obtained from the proposed model was approximately 17.6% higher than that obtained from the conventional model. This can be confirmed using the FFT analysis results of the cogging torques obtained from both models, as shown in Figure 5b. Moreover, the results showed that the 12th harmonic component was the most dominant, as its amplitude obtained from the proposed model was higher, thereby increasing the peak-to-peak cogging torque, than that obtained from the conventional model.

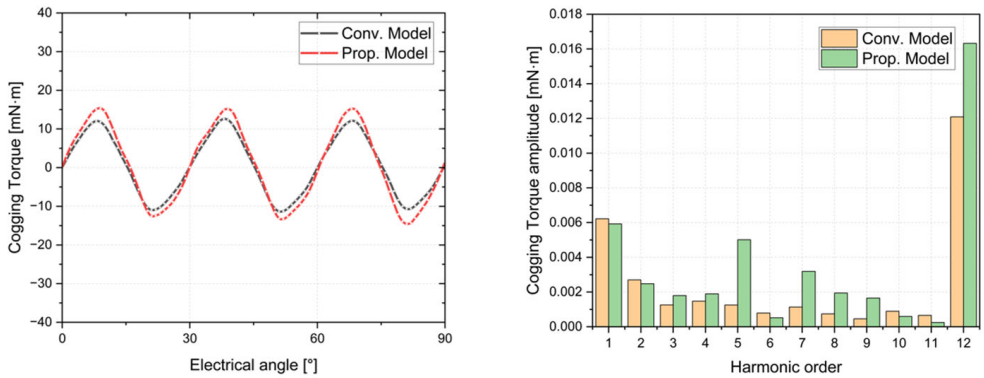

(**a**) (**b**)

Figure 5. Comparison of the (**a**) cogging torque waveforms and the (**b**) FFT results obtained from the two models.

The no-load analysis results show that the phase back-EMF of the proposed model (10.3 V) is slightly higher but comparable to that of the conventional model (10.2 V). It is observed that the phase back-EMF THD and the peak-to-peak cogging torque increased by 0.56% and 17.6%, respectively, relative to the conventional model. However, the THD remains below 5%, which is widely regarded as an acceptable distortion level for sinusoidal voltage waveforms in AC systems and thus indicates a practically sinusoidal back-EMF quality [27]. In addition, the cogging torque is still lower than those reported for other UAV propulsion motors in the literature, as listed in Table 2. Therefore, the no-load performance of the proposed toroidal-winding WRSM can still be regarded as acceptable for UAV propulsion despite the slight degradation in THD and cogging torque relative to the conventional design. The no-load analysis results obtained from the two models are listed in Table 3.

$$V_{THD} = \frac{\sqrt{V_2^2 + V_3^2 + V_4^2 + \ldots + V_n^2}}{V_1}, \tag{13}$$

where V_{THD} is the THD of the phase EMF and, V_1 and V_n represent the fundamental and n-th harmonic components of the back EMF, respectively.

$$K_{cogging} = \frac{360^\circ}{LCM(n_p,\ n_s)} \tag{14}$$

where $K_{cogging}$ is the period of the cogging torque in mechanical degrees, LCM is the least common multiple, and n_p and n_s represent the number of poles and slots, respectively.

Table 2. Comparison of cogging torque values for various UAV propulsion motors reported in the literature.

References	Unit	Cogging Torque
[28]	mN·m	550
[29]	mN·m	60
[30]	mN·m	320
[31]	mN·m	60
[32]	mN·m	57.4

Table 3. No-load analysis results obtained from the conventional and proposed models.

Parameters	Unit	Conventional Model	Proposed Model
Back EMF	V_{rms}	10.2	10.3
THD of the back EMF	%	2.64	3.20
Cogging torque	mN·m	24.4	28.7

3.2. Load Analysis Results

The load analysis was conducted at the rated speed of 3000 rpm by applying the field and armature currents listed in Table 1. The torque equation of the WRSMs is expressed as Equation (15), which represents the sum of the magnetic torque and reluctance torque. The measured average torque values obtained from the two models are 2.32 N·m and 2.33 N·m, respectively, as displayed in Figure 6a, revealing that both models have comparable torque performances. However, the torque ripple, which affects vibration and noise levels, of the proposed model was approximately 1.3% higher than that of the conventional model. This increase was attributed to the higher peak-to-peak cogging torque of the proposed model than that of the conventional model, observed during no-load analysis. Furthermore, a comparison of the magnetic flux line distributions of the two models, displayed in Figure 6b, demonstrates that the flux lines in the proposed model tend to concentrate near the outer tooth region of the stator core. Therefore, the flux path of the proposed model was less uniform than that of the conventional model. The maximum output powers of the conventional and proposed models were 3.52 kW and 3.59 kW, respectively.

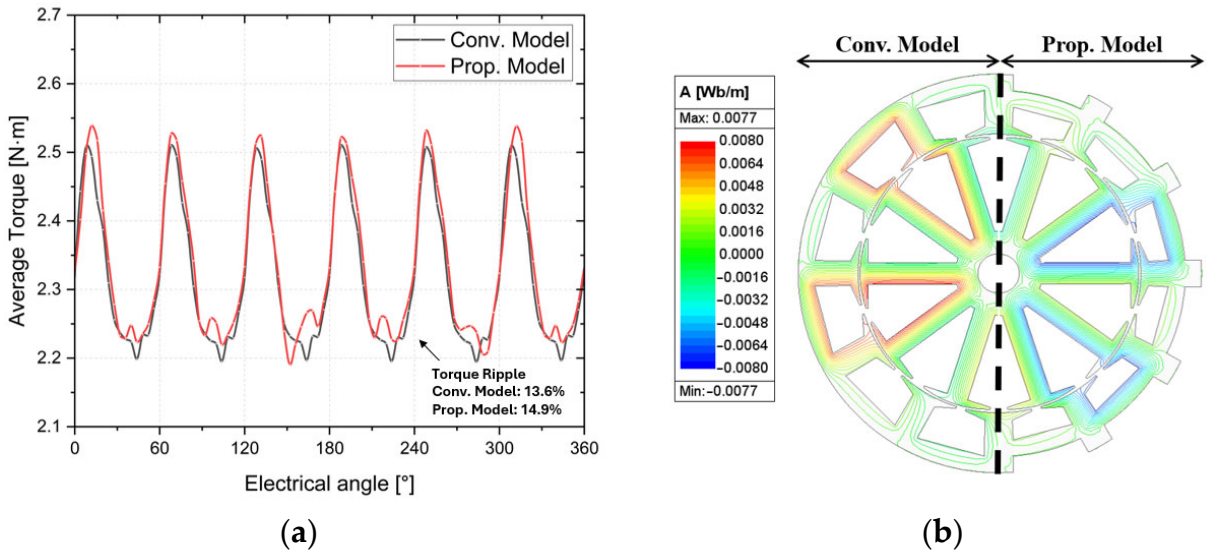

(**a**) (**b**)

Figure 6. Comparison of the (**a**) average torque waveforms and (**b**) magnetic flux lines of the two models.

Figure 7a,b compare the results of the core and eddy current losses of the two models, respectively. As discussed in Section 2.3, the stator core volume of the proposed model decreased by approximately 4.73% relative to that of the conventional model. Consequently, the loss values of the proposed model were confirmed to be lower than those of the conventional one. The efficiency of the motor was calculated based on the load analysis results, revealing that the efficiency of the proposed model improved by approximately 1.9% relative to that of the conventional model due to the reduction in losses. The load analysis results for the two models are listed in Table 4. In addition, the torque and output characteristics of both models over a wide speed range were analyzed, and the results are presented in Figure 8. Both models satisfied the required torque and output characteristics across the entire operating range and were found to show generally similar performance.

$$T = \frac{3}{2}\frac{P}{2}(\lambda_f i_q + (L_d - L_q) i_d i_q), \tag{15}$$

where P is the number of poles, λ_f is the d-axis flux linkage generated by the field current, i_d and i_q are the d- and q-axis currents, respectively, and L_d and L_q are the d- and q-axis inductances, respectively.

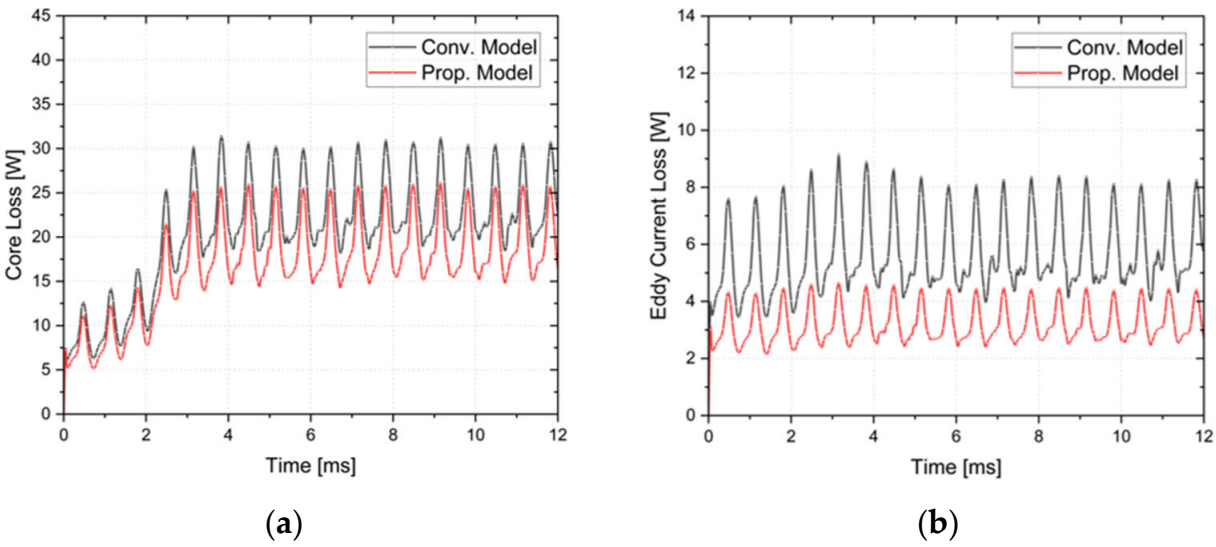

Figure 7. Comparison of the (**a**) core and (**b**) eddy current loss waveforms of the two models.

Table 4. Load analysis results of the conventional and proposed models.

Parameters	Unit	Conventional Model	Proposed Model
Armature current	A	26.5	26.5
Field current	A	10	10
Armature copper loss	W	61.1	44.2
Field copper loss	W	122	122
Core loss	W	23.4	19
Eddy current loss	W	5.76	4.68
Total loss	W	212	190
Average torque	N·m	2.32	2.33
Speed	rpm	3000	3000
Output power	W	729	732
Input power	W	941	922
Efficiency	%	77.5	79.4

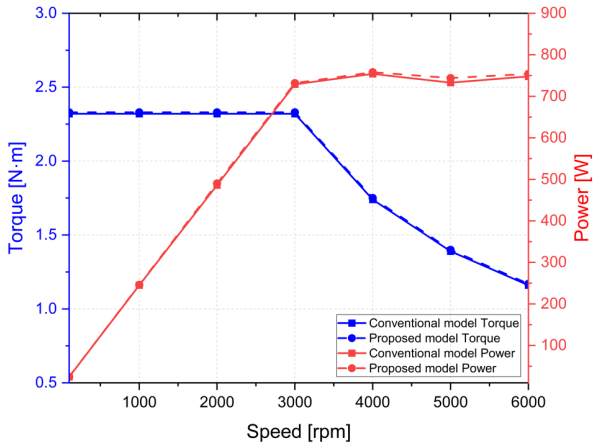

Figure 8. Comparison of wide speed range characteristics of two models.

3.3. Structural Analysis

The rotor was structurally analyzed using ANSYS Mechanical, version 2024 R1, to evaluate structural stability under high-speed operating conditions. To ensure a sufficient safety margin, structural analysis was performed at 7200 rpm, which is higher than the maximum speed. The material properties of the electrical steel and copper used for the structural analysis are listed in Table 5. The equivalent density of copper was used, determined by dividing the total mass of the winding, including the end-turn, by the slot volume of the rotor [33].

Table 5. Material properties.

Parameters	Unit	35PN440	Copper
Density (equivalent density)	kg/m^3	7700	8960 (6498)
Poisson's ratio	-	0.25	0.34
Young's modulus	GPa	195	130
Yield strength	MPa	273	-

The boundary conditions used in the structural analysis are displayed in Figure 9. The structural analysis results confirmed that a maximum stress of 4.5 MPa was generated near the rotor shaft. Consequently, the safety factor, defined as the ratio of the allowable stress to the maximum working stress, was calculated to be 60.6, confirming a high degree of structural safety.

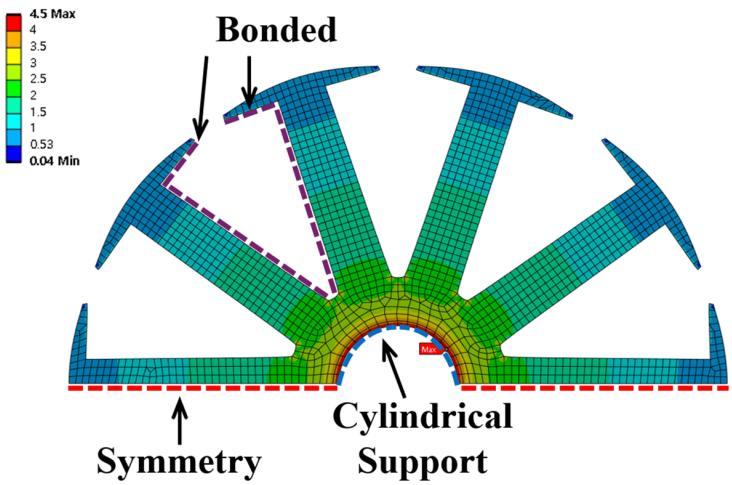

Figure 9. Structural analysis results.

4. Discussion

This section discusses the main differences between the conventional tooth-coil winding WRSM and the proposed toroidal-winding WRSM, and interprets their impact on UAV propulsion performance.

In the conventional model, tooth-coil windings are placed around each stator tooth, so an increase in stator outer diameter or tooth width directly leads to longer end-turns and higher end-turn resistance. In contrast, the proposed model employs a toroidal winding that is wound continuously along the inner and outer stator yokes, which makes it particularly advantageous for machines with a thin stator yoke or short stack length, because the end-turn length can be significantly reduced. In this study, to ensure an objective comparison, the main geometrical parameters such as rotor configuration, stack length, and stator outer diameter were kept identical for both models, so that the effect of the winding topology could be isolated.

As a result of the shorter end-turns in the proposed model, the armature winding copper loss is reduced by about 28% compared with the conventional tooth-coil design. Furthermore, the reduction in stator core volume and total conductor length in the proposed topology leads to decreases in core loss, eddy-current loss, and copper loss, which together yield an efficiency improvement of approximately 1.9% over the conventional model. These improvements are particularly beneficial for UAV propulsion, where higher efficiency directly contributes to longer flight time and better energy utilization.

The modified stator geometry introduced to accommodate the toroidal winding reduces the stator volume and alters the flux paths compared with the conventional design. In the proposed model, the magnetic flux tends to concentrate toward the outer tooth region of the stator core, so the air-gap flux distribution becomes less uniform than in the conventional machine. This slightly more asymmetric flux pattern strengthens certain space harmonics in the air-gap field, which in turn leads to higher back-EMF THD and an increased peak-to-peak cogging torque at no load. The THD of the phase back-EMF and the peak-to-peak cogging torque of the proposed model are increased by 0.56% and 17.6%, respectively, relative to the conventional machine. At the same time, the reduced stator volume and shortened end-turn winding region lower the core and copper losses, resulting in an efficiency improvement from 77.5% to 79.4% under load. Consequently, the THD remains below 5%, and the cogging torque is still lower than those reported for other UAV propulsion motors. Given that efficiency under load condition is more critical than no-load condition indices in this application, the proposed toroidal-winding WRSM is regarded as an advantageous alternative for UAV propulsion.

Finally, a comprehensive analysis over the full operating range confirms that both models satisfy the required torque and output power across the considered speed and load conditions, exhibiting broadly similar overall performance. Within this context, the proposed toroidal-winding WRSM offers a favorable trade-off by achieving substantially lower losses and higher efficiency while maintaining comparable torque capability to the conventional tooth-coil WRSM, at the expense of a modest degradation in no-load smoothness metrics that remain tolerable for UAV applications.

5. Conclusions

This study proposed non-permanent magnet type WRSMs for application as propulsion motors for UAVs. Specifically, a model with a toroidal winding was introduced to enhance motor efficiency by reducing winding resistance. To analyze performance, a conventional model with a tooth-coil winding and the proposed model with a toroidal winding were designed, and their characteristics were compared using an FEA software ANSYS Maxwell 2D, version 2024 R1. The proposed model with a toroidal winding demonstrated

a total loss reduction of approximately 10.4% relative to the conventional tooth-coil model, increasing efficiency by 1.9%. Mechanical analysis further validated the structural robustness of the rotor under high-speed conditions, confirming the feasibility of the proposed design for application in UAV propulsion. In future work, the no-load characteristics, such as back-EMF THD and cogging torque, as well as the torque ripple under load will be further improved by optimizing electromagnetic design parameters, including the stator tooth and yoke dimensions, slot opening and shape, and rotor pole and shoe geometry.

Author Contributions: Model design, analysis, and writing, S.-E.K.; review and editing, Y.-M.Y. All authors have read and agreed to the published version of the manuscript.

Funding: This result was supported by the "Regional Innovation System & Education (RISE)" through the Gwangju RISE Center, funded by the Ministry of Education (MOE) and the Gwangju Metropolitan Government, Republic of Korea. (2025-RISE-05-011), and by Basic Science Research Program through the National Research Foundation of Korea (NRF) funded by the Ministry of Education (RS-2025-25398164).

Institutional Review Board Statement: Not applicable.

Informed Consent Statement: Not applicable.

Data Availability Statement: All data generated or analyzed during this study are included in this article. Further information or requests for data access can be directed to the corresponding author.

Conflicts of Interest: The authors declare no conflicts of interest.

Abbreviations

The following abbreviations are used in this manuscript:

UAV	Unmanned aerial vehicles
SPMSMs	Surface-mounted permanent magnet synchronous motors
WRSMs	Wound-rotor synchronous motors
SRMs	Switched reluctance motors
PMSMs	Permanent magnet synchronous motors
THD	Total harmonic distortion
TRV	Torque per unit rotor volume
FEA	Finite element analysis
EMF	Electromotive force
FFT	fast Fourier transform
LCM	Least common multiple

References

1. Xu, J.; Jin, W.; Lin, H.; Zhang, B.; Guo, H. Multiobjective Optimization Method to Maximize Power Density and Efficiency of an Electric Propulsion Motor in UAV Applications. *IEEE Trans. Transp. Electrif* **2024**, *10*, 5484–5494. [CrossRef]
2. Abro, G.E.M.; Zulkifli, S.A.B.M.; Masood, R.J.; Asirvadam, V.S.; Laouiti, A. Comprehensive Review of UAV Detection, Security, and Communication Advancements to Prevent Threats. *Drones* **2022**, *6*, 284. [CrossRef]
3. Zong, J.; Zhu, B.; Hou, Z.; Yang, X.; Zhai, J. Evaluation and Comparison of Hybrid Wing VTOL UAV with Four Different Electric Propulsion Systems. *Aerospace* **2021**, *8*, 256. [CrossRef]
4. Popa, D.-C.; Szabó, L. Securing Rare Earth Permanent Magnet Needs for Sustainable Energy Initiatives. *Materials* **2024**, *17*, 5442. [CrossRef]
5. An, Q.; Lu, Y.; Zhao, M. Review of Key Technologies of the High-Speed Permanent Magnet Motor Drive. *Energies* **2024**, *17*, 5252. [CrossRef]
6. Ebrahimi, B.M.; Faiz, J. Demagnetization Fault Diagnosis in Surface Mounted Permanent Magnet Synchronous Motors. *IEEE Trans. Magn.* **2013**, *49*, 1185–1192. [CrossRef]
7. Oksuztepe, E.; Ural Bayrak, Z.; Kaya, U. Effect of flight level to maximum power utilization for PEMFC/supercapacitor hybrid uav with switched reluctance motor thruster. *Int. J. Hydrog. Energy* **2023**, *48*, 11003–11016. [CrossRef]

8. Vigneshwar, S.T.; Balaji, M.; Prabhu, S. Comparative Analysis of PMSMs and SRMs for Drone Applications. *Eng. Proc.* **2025**, *93*, 14.
9. Biczyski, M.; Sehab, R.; Whidborne, J.F.; Krebs, G.; Luk, P.C.K. Fault-tolerant switched reluctance motor propulsion system for eVTOLs. *J. Phys. Conf. Ser.* **2023**, *2526*, 012065. [CrossRef]
10. Seo, H.-S.; Park, C.-B.; Kim, S.-H.; Lei, G.; Guo, Y.; Lee, H.-W. Utilizing MicroGenetic Algorithm for Optimal Design of Permanent-Magnet-Assisted WFSM for Traction Machines. *Appl. Sci.* **2024**, *14*, 5150. [CrossRef]
11. Kim, H.-V.; Kim, D.-H.; Lee, J.-S. Comparison of Flux-Weakening Control Methods for Wound Field Synchronous Motor. In Proceedings of the 2024 IEEE Applied Power Electronics Conference and Exposition (APEC), Long Beach, CA, USA, 25–29 February 2024.
12. Kim, Y.; Nam, K. Copper-Loss-Minimizing Field Current Control Scheme for Wound Synchronous Machines. *IEEE Trans. Power Electron.* **2017**, *32*, 1335–1345. [CrossRef]
13. Oh, H.-J.; Cho, J.-H.; Hwang, Y.-H.; Kim, Y.; Jung, S.-W.; Jung, S.-Y. Performance Improvement of Wound Field Synchronous Motor for EV Propulsion Applying Grain-Oriented Electrical Steel. *IEEE Trans. Magn.* **2025**, *61*, 8200704. [CrossRef]
14. Park, H.-J.; Lim, M.-S. Design of High Power Density and High Efficiency Wound-Field Synchronous Motor for Electric Vehicle Traction. *IEEE Access* **2019**, *7*, 46677–46685. [CrossRef]
15. Zou, T.; Li, D.; Qu, R.; Li, J.; Jiang, D. Analysis of a Dual-Rotor, Toroidal-Winding, Axial-Flux Vernier Permanent Magnet Machine. *IEEE Trans. Ind. Appl.* **2017**, *53*, 1920–1930. [CrossRef]
16. Aoyama, M.; Tsuya, H.; Hirata, S.; Sjöberg, L. Experience of Toroidally Wound Double Rotor Axial-Gap Induction Machine With Soft Magnetic Composites. *IEEE Open J. Ind. Appl.* **2021**, *2*, 378–393. [CrossRef]
17. De Donato, G.; Giulii Capponi, F.; Caricchi, F. Fractional-Slot Concentrated-Winding Axial-Flux Permanent-Magnet Machine With Core-Wound Coils. *IEEE Trans. Ind. Appl.* **2012**, *48*, 630–641. [CrossRef]
18. Spargo, C.; Mecrow, B.; Widmer, J. Synchronous Reluctance Motors with Toroidal Windings. In Proceedings of the 2014 IEEE Energy Conversion Congress and Exposition (ECCE), Pittsburgh, PA, USA, 14–18 September 2014.
19. Hanselman, D.C. *Brushless Permanent Magnet Motor Design*, 2nd ed.; Magna Physics Publishing: Orono, ME, USA, 2003; pp. 110–111.
20. Zhao, W. Design of Novel Dual-Airgap Spoke-Type Permanent Magnet Machines with Phase-Group Concentrated-Coil Windings. Ph.D. Thesis, Hanyang University, Seoul, Republic of Korea, 2015.
21. Terao, Y.; Okumura, S.; Ohsaki, H. Study on Electric and Magnetic Loadings in Fully Superconducting Motor Design. *Phys. C Supercond. Appl.* **2024**, *617*, 1354399. [CrossRef]
22. Graffeo, F.; Vaschetto, S.; Tenconi, A.; Cavagnino, A. Fast Sizing Procedure for Salient-Pole Wound Field Synchronous Motors for Transportation Electrification. In Proceedings of the 2023 IEEE International Electric Machines & Drives Conference (IEMDC), San Francisco, CA, USA, 15–18 May 2023.
23. Zhao, W.; Shen, H.; Fan, X.; Wang, X.; Kwon, B. Design and analysis of a novel hybrid-excited wound-rotor synchronous machine with high electromagnetic performance. *Int. J. Appl. Electromagn. Mech.* **2019**, *59*, 745–753. [CrossRef]
24. Graffeo, F. Design and Analysis of Different Rotor Configurations for Wound Field Synchronous Machines. Master's Thesis, Politecnico di Torino, Torino, Italy, 2020.
25. He, T.R.; Xu, F.; Zhu, Z.Q.; Liang, D.; Bin, H.; Wu, D.; Gong, L.M.; Chen, J.T. Comparison of Toroidal and Tooth-Coil Winding 2-Pole Slotted High-Speed Permanent Magnet Motors. *IEEE Trans. Ind. Appl.* **2024**, *60*, 3870–3882. [CrossRef]
26. Lee, H.-Y.; Yoon, S.-Y.; Kwon, S.-O.; Shin, J.-Y.; Park, S.-H.; Lim, M.-S. A Study on a Slotless Brushless DC Motor with Toroidal Winding. *Processes* **2021**, *9*, 1881. [CrossRef]
27. *IEEE Std 519-2014*; IEEE Recommended Practice and Requirements for Harmonic Control in Electric Power Systems. IEEE: New York, NY, USA, 2014.
28. de la Cruz Soto, J.; Gascon-Avalos, J.J.; Rumbo-Morales, J.Y.; Ortiz-Torres, G.; Zurita-Gil, M.A.; Sorcia-Vázquez, F.D.J.; Pérez-Ramírez, J.; Valle-López, O.A.; Garcia-Castro, S.E.; Buenabad-Arias, H.M.; et al. Analysis and Assessment of a Brushless DC Outrunner Motor for Agriculture Drones Using JMAG. *Appl. Syst. Innov.* **2025**, *8*, 81. [CrossRef]
29. Liu, C.; Yu, J.; Lee, C.H.T. A New Electric Magnetic-Geared Machine for Electric Unmanned Aerial Vehicles. *IEEE Trans. Magn.* **2017**, *53*, 8111306. [CrossRef]
30. Ghods, M.; Faiz, J.; Bazrafshan, M.A.; Gorginpour, H.; Toulabi, M.S. Design of an L-Shaped Array Vernier Permanent Magnet Machine for Unmanned Aerial Vehicle Propulsion Using a Schwarz–Christoffel Mapping-Based Equivalent Magnetic Network Model. *IEEE Trans. Ind. Electron.* **2024**, *71*, 237–249. [CrossRef]
31. Sundaramoorthy, P.; Devireddy, P.; Thummala, C.; Valmiki, S.; Kaperla, P.A.; Padmanabhan, D. PMSM Motors in the Air: Investigating Torque Characteristics for Optimal Drone Performance. In Proceedings of the 2024 IEEE Third International Conference on Power Electronics, Intelligent Control and Energy Systems (ICPEICES), Delhi, India, 26–28 April 2024.

32. Lee, J.-K.; Lee, S.-H.; Kim, Y.-S. A Study on Design of Torque Motor for Drone Gimbal System. In Proceedings of the 2018 21st International Conference on Electrical Machines and Systems (ICEMS), Jeju, Republic of Korea, 7–10 October 2018.
33. Park, M.-R.; Kim, D.-M.; Jung, Y.-H.; Lim, M.-S. High energy efficiency oriented-control and design of WFSM based on driving condition of electric vehicle. *Mechatronics* **2022**, *81*, 102696. [CrossRef]

Disclaimer/Publisher's Note: The statements, opinions and data contained in all publications are solely those of the individual author(s) and contributor(s) and not of MDPI and/or the editor(s). MDPI and/or the editor(s) disclaim responsibility for any injury to people or property resulting from any ideas, methods, instructions or products referred to in the content.